MOMENT MODEL OF NONUNIFORM CHANNEL-BEND FLOW. I: FIXED BEDS

By Keh-Chia Yeh,[1] Associate Member, ASCE, and
John F. Kennedy,[2] Member, ASCE

ABSTRACT: A nonuniform, fixed-boundary, channel-bend flow is formulated as two coupled sets of equations, each comprising two simultaneous equations, derived from the cross-section–integrated equations (in circular cylindrical coordinates) of conservation of flux of moment of momentum, and the depth-integrated momentum and continuity equations. Boundary shear stresses are related to the primary-flow shear stress and the primary and secondary velocities. The equations are solved numerically and the results found to be in satisfactory agreement with experimental data. The moment formulation elucidates the interplay among the secondary and primary flows, notably the observed flattening of primary velocity profiles, overshoot of the secondary flow, radial redistribution of the depth-averaged primary velocity, and the secondary translational velocity. The erodible-bed case is treated in the companion paper.

INTRODUCTION

The hybrid integral-differential formulation developed herein treats flow from a straight channel into and through a constant-radius bend, and then into another straight channel, as shown in Fig. 1. In this paper the channel section is treated as rectangular and fixed. The analysis is extended in part II (Yeh and Kennedy 1993) to the case of erodible-bed, fixed-wall channels, and reveals several features of this flow that differ significantly from the fixed-bed case. Many natural meandering river channels can be accurately described as series of practically constant-radius bends connected by relatively short intervening reaches of nearly straight channel, and therefore the analytical results obtained in the companion paper are applicable to finite-amplitude river meanders. The integrated (over a control volume extending across the full channel cross section and an incremental distance $r \cdot d\theta$ along the channel) equations for the flux of moment of momentum are utilized to formulate the secondary (radial-plane) rotational flow and the effects of curvature on the primary-flow velocity profile. The depth-averaged primary and the secondary (radial-plane) translational flow (which is different from the secondary rotational flow) are formulated from the depth-integrated differential momentum and continuity equations. This formulation is, in several respects, an extension of Vadnal's (1984) analysis. Complete details of the formulation and more extensive verification are presented by Yeh (1990).

The approach presented herein contrasts the work of Johannesson and Parker (1989), Struiksma et al. (1985), and Blondeaux and Seminara (1985). The approach includes a calculation of the change the primary flow velocity profile undergoes as the flow passes along a bend.

---

[1]Assoc. Prof., Dept. of Civ. Engrg., Nat. Chiao Tung Univ., Hsinchu, Taiwan 30050, Republic of China.

[2]Deceased; formerly, Hunter Rouse Prof. of Hydr. and Dir., Inst. of Hydr. Res., Univ. of Iowa, Iowa City, IA 52242-1585.
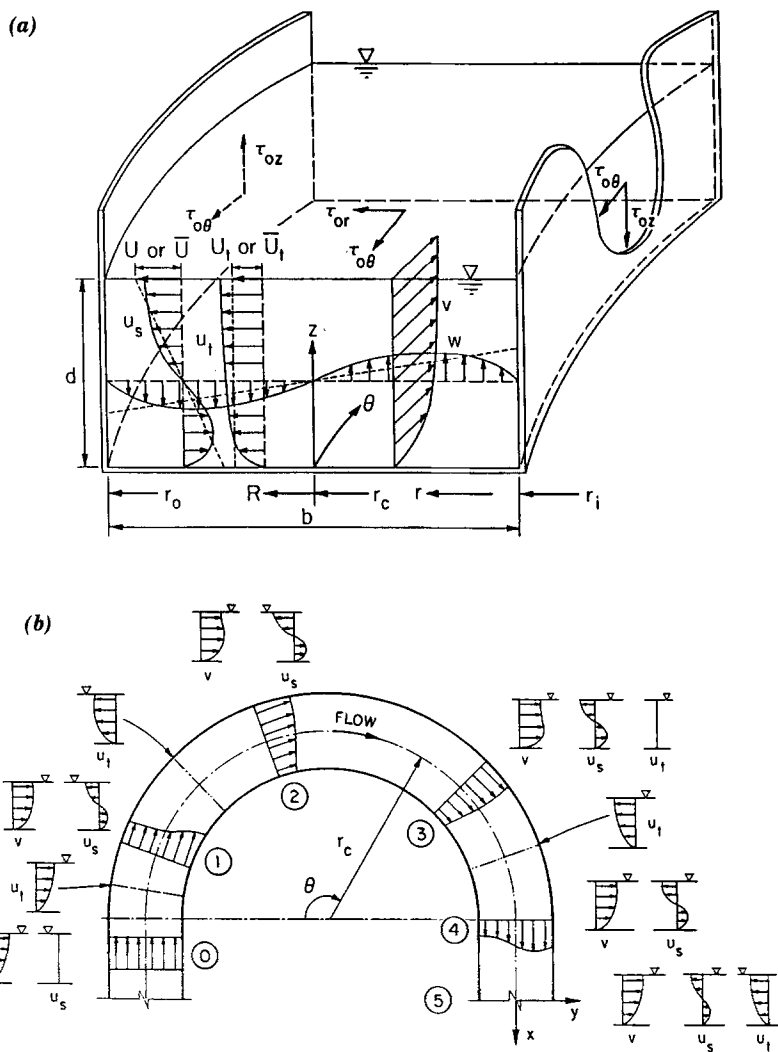
FIG. 1. Channel-Bend Flow (Radial-Plane Velocity Profiles Viewed from Upstream; Dashed Profiles Represent Idealizations Utilized in Integral Formulation)

PHYSICAL DESCRIPTION

The fixed-boundary bend flow described here is depicted in Fig. 1. The channel comprises a straight, uniform-flow (far upstream) approach reach, that is followed by a constant-width, constant-radius curve that discharges into a long, straight uniform channel.

It is useful in the following description to have available the equations of motion and continuity for circular cylindrical coordinates. For steady, incompressible flow, these are

777

$$\rho \left(u \frac{\partial u}{\partial r} + \frac{v}{r} \frac{\partial u}{\partial \theta} - \frac{v^2}{r} + w \frac{\partial u}{\partial z} \right) = \rho g_r + \frac{1}{r} \frac{\partial(r\sigma_{rr})}{\partial r} - \frac{\sigma_{\theta\theta}}{r} + \frac{1}{r} \frac{\partial \tau_{r\theta}}{\partial \theta} + \frac{\partial \tau_{rz}}{\partial z}$$
$$\cdots \cdots \cdots (1)$$

$$\rho \left(u \frac{\partial v}{\partial r} + \frac{v}{r} \frac{\partial v}{\partial \theta} + \frac{uv}{r} + w \frac{\partial v}{\partial z} \right) = \rho g_\theta + \frac{1}{r^2} \frac{\partial(r^2\tau_{r\theta})}{\partial r} + \frac{1}{r} \frac{\partial \sigma_{\theta\theta}}{\partial \theta} + \frac{\partial \tau_{\theta z}}{\partial z} \cdots (2)$$

$$\rho \left(u \frac{\partial w}{\partial r} + \frac{v}{r} \frac{\partial w}{\partial \theta} + w \frac{\partial w}{\partial z} \right) = \rho g_z + \frac{1}{r} \frac{\partial(r\tau_{rz})}{\partial r} + \frac{1}{r} \frac{\tau_{\theta z}}{\partial \theta} + \frac{\partial \sigma_{zz}}{\partial z} \cdots \cdots (3)$$

$$\frac{1}{r} \frac{\partial(ru)}{\partial r} + \frac{1}{r} \frac{\partial v}{\partial \theta} + \frac{\partial w}{\partial z} = 0 \cdots \cdots \cdots \cdots (4)$$

where, in addition to the quantities defined in Fig. 1, ρ = fluid density; (u, v, w) = (r, θ, z) components of velocity; $\rho g_{r,\theta,z}$ = components of gravitational body force in the coordinate directions; $\sigma_{ii} = -p + \tau_{ii}$ = normal stress; p = pressure; and τ_{ij} = shear stress. It can be shown by means of an ordering analysis (Yen 1965) that several of the terms (1)–(3) are of higher order and can be neglected.

The secondary rotational flow will be described first. The primary velocity, $v(r, \theta, z)$, is nonuniformly distributed vertically, and hence so also is the radial acceleration [represented by the terms on the left side of (1)]. The radial forces produced by the radial accelerations are referred to as radial-acceleration forces; and the sum of the θ moments (about, say, the section centroid) produced by the radial-acceleration forces corresponding to the acceleration terms on the left sides of (1) and (3) as the acceleration moment. The radial-acceleration forces are resisted principally by the radial gradient of σ_{rr} [included in the term $(1/r)[\partial(r\sigma_{rr})/\partial r]$, in (1)] which is produced by the radial inclination, S_s, of the water surface and is nearly constant over the depth. The difference between the vertical distributions of the radial-acceleration and pressure-gradient forces produces a net radial force (per unit mass or volume of fluid) at any elevation in the $+r$ ($-r$) direction over the upper (lower) part of the flow. The integral over the depth of the difference between these two forces is nearly zero (the small difference is balanced by the radial bed-shear force), but the local (at any elevation) difference between them is significant and produces a moment about the section centroid that in turn produces the secondary rotational velocity u_s, shown in Fig. 1.

For a rectangular channel, the acceleration moment, dm_θ, exerted about the section centroid on a control volume extending over the whole cross section and subtending an element of arc length $r \cdot d\theta$ is

$$dm_\theta = \rho \int_0^d \int_{r_i}^{r_0} \left[\left(z - \frac{d}{2} \right) \left(\frac{v}{r} \frac{\partial u}{\partial \theta} - \frac{v^2}{r} \right) \right.$$
$$\left. + (r - r_c) \left(u \frac{\partial w}{\partial r} + \frac{v}{r} \frac{\partial w}{\partial \theta} \right) \right] r \, dr \, dz \, d\theta \cdots \cdots \cdots \cdots (5)$$

where the origin of the coordinate system is at the channel bottom. The centrifugal term, v^2/r, is dominant in (5). The net pressure force [σ_{rr} and $\sigma_{\theta\theta}$ in (1), whose integral over the depth almost balances the radial-accel-

778

eration force] is very nearly constant over the depth, and produces no moment about the section centroid. The lateral inclination of water surface is sufficiently small that flow depth can be assumed constant.

The secondary rotational flow is resisted by the radial-plane boundary shear stresses, τ_{0r} and τ_{0z}. For fully developed curved-channel flow, the moment dm_τ due to these boundary shear stresses just balances the acceleration moment given by (5). In the case of nonuniform flow (e.g., around sections 1 and 4 in Fig. 1), it is helpful to visualize the moment corresponding to the centrifugal term, v^2/r, as the driving or centrifugal moment, and that corresponding to terms $(v/r)(\partial u/\partial\theta)$, $u(\partial w/\partial r)$, and $(v/r)(\partial w/\partial\theta)$ as the inertial moment. The last term is analogous to the rotational inertia of a rotating rigid body. Within reaches of nonuniform flow, the centrifugal moment is balanced by the inertial and boundary-shear-stress moments.

Another aspect of bend flow that is conveniently viewed in terms of moments is the effect of flow curvature on the primary-flow velocity profile, $v(\theta, z)$, and the interplay between the θ- and r-components of the flow rotation. For the present discussion $\partial v/\partial r = 0$ will be assumed. Fig. 2 portrays the θ fluxes of moment of momentum (MOM) and the moments for a cross-sectional control volume of the flow. The components M_r and M_θ of MOM are due to the primary flow and secondary rotational flow, respectively, and are directed along the r- and θ-axes. The flux of MOM across any surface is given by

$$\mathbf{M} = \int_{cs} \rho(\mathbf{r} \times \mathbf{q})(\mathbf{q} \cdot d\mathbf{A}) \quad \dots\dots\dots\dots\dots\dots\dots\dots\dots\dots\dots\dots\dots\dots \quad (6)$$

where $d\mathbf{A}$ = vector pointing inward and normal to the surface element dA

$$\mathbf{r} = r\mathbf{e}_r + r \cdot d\theta\mathbf{e}_\theta + z\mathbf{e}_z \quad \dots\dots\dots\dots\dots\dots\dots\dots\dots\dots\dots\dots\dots \quad (7)$$

and

$$\mathbf{q} = u\mathbf{e}_r + v\mathbf{e}_\theta + w\mathbf{e}_z \quad \dots\dots\dots\dots\dots\dots\dots\dots\dots\dots\dots\dots\dots\dots \quad (8)$$

The r- and θ-components of $\mathbf{M}$ across the radial planes bounding the control volume, obtained from (6)–(8), are

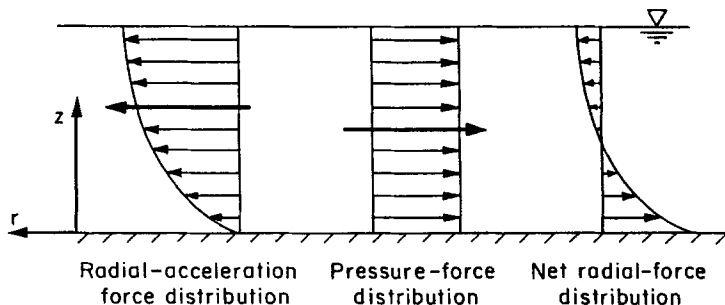$$M_r = -\rho \int_A zv^2 \, dA \quad \dots\dots\dots\dots\dots\dots\dots\dots\dots\dots\dots\dots\dots\dots\dots \quad (9)$$

Radial–acceleration force distribution   Pressure–force distribution   Net radial–force distribution

FIG. 2. Conservation of Horizontal-Plane Flux of Moment of Momentum

779

$$M_\theta = \rho \int_A v(zu - rw) \, dA \quad \dots\dots\dots\dots\dots\dots\dots\dots\dots\dots\dots\dots \quad (10)$$

M_r arises from the vertically nonuniform distribution of v; and M_θ primarily from the nonuniform distributions of v and u, and secondarily from the sign reversal of w.

The conservation of MOM formulated in Fig. 2 illustrates some important features of bend flow. First, M_θ is augmented by the MOM influx from $M_r \cdot d\theta$, and is diminished by the boundary-shear-stress moment, dm_τ, and by the pressure moment, dm_p, resulting from the pressure difference between the walls (the section-centroid moment of which is almost zero for the fixed-bed case). Second, M_r is reduced by the interaction of the secondary current and the curvature of the primary flow ($M_\theta \cdot d_\theta$ in Fig. 2); and is augmented by dm_n, which results from the decrease of M_r and is discussed in the next paragraph. Reduction of M_r is manifested by the v profile becoming more uniform; i.e., by a reduction of $\partial v/\partial z$. As a matter of fact, some experimental data (Rozovskii 1961) for flow in sharply curved channels (those with large b/r_c) show that the primary velocity profile can become inverted, with the larger velocities occurring in the lower part of the flow, as shown in sections 2 and 3 in Fig. 1.

The displacement of the vertical distribution of v from its equilibrium profile gives rise to a radial restoring moment, denoted by dm_n in Fig. 2. The underlying mechanics are illustrated in Fig. 3, which includes equilibrium (solid line) and displaced (dashed line) velocity profiles, and the corresponding distributions of $\tau_{z\theta}$ ($= \tau_{\theta z}$). Note that for this comparison, both velocity profiles are taken to have the same depth-averaged value, and to produce equal boundary shear stresses, $\tau_{0\theta}$. The distribution of the eddy viscosity, $\varepsilon(z)$, can therefore be assumed to be the same for both velocity profiles, because the turbulence configuration and hence also ε are deter-
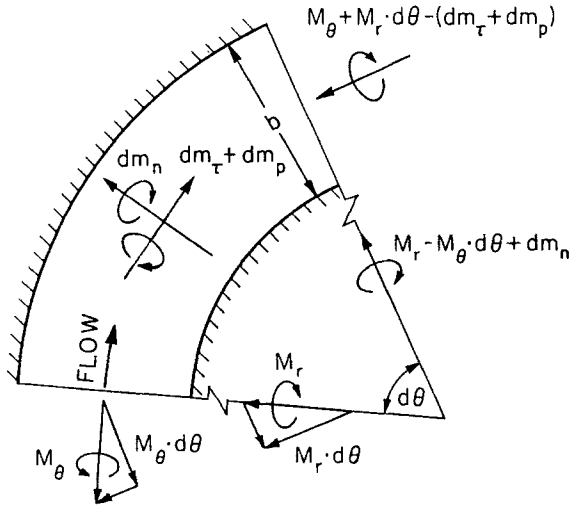

FIG. 3. Equilibrium (——) and Nonequilibrium (-----) Distributions of v and $\tau_{\theta z}$; and Resultant Radial Moment dm_n for Nonequilibrium Open-Channel Flow

mined principally by the boundary shear stress. For the equilibrium situation, the dominant moments about the centroid of the control volume are produced by the shear stresses $\tau_{\theta\theta}$ and $\tau_{\theta z}$, and are just in balance for a linear distribution of $\tau_{\theta z}$. For the flatter, nonequilibrium profile, with $\tau_{\theta z}$ expressed by the Boussinesq relation

$$\tau_{\theta z} = \rho\varepsilon \frac{\partial v}{\partial z} \dots\dots\dots\dots\dots\dots\dots\dots\dots\dots\dots\dots\dots\dots\dots (11)$$

the moment about the centroid due to $\tau_{\theta z}$ is reduced, because the integral of $\varepsilon \, \partial v/\partial z$ over the depth is smaller for the flatter profile. The resulting moment acting on a control volume of dimensions d, b, and $r \cdot d\theta$ (see Fig. 3) is

$$dm_n = \int_0^d \int_{r_i}^{r_o} \rho\varepsilon \frac{\partial v}{\partial z} r \, dr \, dz \, d\theta - \int_{r_i}^{r_o} \tau_{\theta\theta} \frac{d}{2} r \, dr \, d\theta \dots\dots\dots\dots\dots (12)$$

The moment due to $\tau_{\theta\theta}$ is greater than that due to the couple produced by $\tau_{\theta z}$, and the resultant clockwise (as viewed in Fig. 3) moment acts to increase the vorticity and the associated MOM, denoted by M_r, of the primary-flow velocity profile and restore the profile toward equilibrium. Note that moments produced by pressure and gravity forces are of higher order and do not enter the moment balance described previously.

Experimental data (Rozovskii 1961; de Vriend 1976; Odgaard and Bergs 1988) reveal that even in reaches of developing and decaying flow (e.g., around sections 1 and 4 in Fig. 1), the local equilibrium transverse water-surface slope, S_s, develops almost immediately, and in a bend whose r_c varies continuously and reasonably slowly with θ can be well approximated at any section by

$$S_s(\theta) = \frac{\bar{V}^2}{gr_c(\theta)} \dots\dots\dots\dots\dots\dots\dots\dots\dots\dots\dots\dots\dots\dots\dots (13)$$

where $\bar{V}$ = section averaged θ velocity. As a result of the streamwise variation of S_s, the flow entering the bend along the right or left (inner or outer) part of the channel (see Fig. 1) experiences increased or diminished, respectively, streamwise pressure gradient, and is accelerated or decelerated accordingly. Thus around section 1 in Fig. 1, the local depth-averaged streamwise velocity, $V(r, \theta)$, is increased across the inner part, and decreased across the outer part, of the channel. Because of water-continuity requirements, this will result in an inward translational velocity, $-u_t$.

The secondary rotational flow advects streamwise momentum toward the outer bank (due to $\partial v/\partial z > 0$), while the secondary translational flow advects streamwise momentum toward the inner bank; both processes are represented by the term $u(\partial v/\partial r)$, in (2). The former is usually larger than the latter except for very sharp bends, and consequently as the flow progresses along the bend the maximum depth-averaged primary velocity shifts from near the inner bank toward the outer bank. To satisfy water continuity, the secondary translational velocity changes direction and becomes directed radially outward. This occurs in the upstream part of the bend (between sections 1 and 2 in Fig. 1). Terms uv/r and $w(\partial v/\partial z)$, in (2), usually have minor contributions in transporting θ-momentum toward the outer bank. The result of the outward transport of θ-momentum is that the radial gradient of V becomes reversed, and after some distance along the bend, $\partial V/\partial r > 0$ (e.g., at sections 2–4 in Fig. 1) except near the outer bank.

781

As the flow passes through the upstream part of the bend, M_r is decreased by the kinematic effect illustrated in Fig. 2 and the v profile becomes flatter, as can be seen from (9). The centrifugal moment is thereby reduced. Along this reach, M_θ is augmented by the influx from $M_r \cdot d\theta$, and restrained by dm_τ (which increases as the secondary flow becomes stronger). The net result of the reduction of the centrifugal moment, the augmentation of M_θ, and the effect of the inertial moment is that the secondary rotational flow can "overshoot" its equilibrium strength, and then diminish toward its uniform-flow value. The decay of the secondary rotational flow is produced by dm_τ and impeded by the inertial moment. Equilibrium secondary rotational flow and fully developed primary flow are achieved, as can be seen in Fig. 2, when $M_r \cdot d\theta$ is just balanced by dm_τ and dm_p; and $M_\theta \cdot d\theta$ equals dm_n. At this stage, u_t becomes zero due to the constancy of V in the θ-direction.

The secondary rotational flow continues practically undiminished up to the end of the bend, and, then decays more or less exponentially along the transition reach downstream from the bend. The centrifugal moment and the radial force that inclines the water surface both abruptly cease at the end of the bend. The resulting increase and decrease of the θ-direction slope of the water surface over the outer and inner parts of the channel act to further increase and decrease V in these respective parts of the flow. Therefore, outward u_t occurs again. The return to a straight-channel equilibrium lateral distribution of V occurs some distance downstream from the end of the bend, and is driven principally by the shear-stress τ_{yx} and advection (by residual secondary current) of x-momentum in the y-direction (see coordinates in Fig. 1).

MATHEMATICAL FORMULATION

Integrated MOM Equations

For the formulation of the integrated MOM equations, specification of the distributions of the several velocities and stresses involved is required, as follows.

The primary velocity, v, is treated as being power-law distributed

$$v = \frac{n+1}{n} \bar{V} \zeta^{1/n} \dots \dots \dots \dots \dots \dots \dots \dots \dots \dots \dots \dots \dots \dots \dots (14)$$

where $\zeta = z/d$; $\bar{V}(\theta)$ = section-averaged v; and $1/n(\theta)$ = power-law exponent.

The secondary-flow velocity comprises two parts (see Fig. 1)

$$u = u_s(\theta, \zeta) + \bar{U}_t(\theta) \dots \dots \dots \dots \dots \dots \dots \dots \dots \dots \dots \dots (15)$$

where u_s = secondary-flow rotational velocity; and $\bar{U}_t$ = radially averaged secondary translational velocity. For the fixed-bed case, the secondary translational velocity is treated as being uniformly distributed over the channel cross section. The secondary rotational velocity for both the fixed- and erodible-bed cases is taken for this integral analysis to be piecewise linearly distributed (dashed u_s profile in Fig. 1)

$$u_s = \bar{U} \frac{(\xi - 1)(\xi - \zeta)}{\xi^2} ; \qquad 0 \le \zeta \le \xi \dots \dots \dots \dots \dots \dots \dots \dots (16a)$$

$$u_s = \bar{U} \frac{\xi - \zeta}{\xi - 1} ; \qquad \xi \le \zeta \le 1 \dots \dots \dots \dots \dots \dots \dots \dots \dots \dots (16b)$$

where $\bar{U}(\theta)$ = surface value of u_s; and $\zeta = \xi$ at which $u_s = 0$. Analytical results (Falcon and Kennedy 1983) and experimental data (Odgaard 1986) suggest $\xi = 0.5$.

The vertical velocity, w, is treated as linearly distributed across the channel (dashed w profile in Fig. 1). Its magnitude at the outer and inner walls will be taken such that continuity is satisfied for each quadrant of the cross section; i.e., the radially inward and outward discharges due to u_s across the vertical section at r_c equal the upward and downward discharges due to w across the horizontal section at $\zeta = \xi$

$$w = \gamma \frac{4\bar{U}d}{b^2} (1 - \xi)(r_c - r) \dots\dots\dots\dots\dots\dots\dots\dots\dots\dots\dots (17)$$

where γ = constant < 1, included to account for w diminishing to zero at the bed, free surface and walls.

The pressure distribution is hydrostatic

$$\sigma_{rr} = \sigma_{\theta\theta} = -\rho g d \left(1 - \zeta + S_s \frac{r - r_c}{d} \right) \dots\dots\dots\dots\dots\dots (18)$$

where S_s = radial-water-surface slope given by (13).

The streamwise component of the bed shear stress is expressed by the Darcy-Weisbach formula

$$\tau_{\theta\theta} = \frac{1}{8} \rho f \bar{V}^2 \dots\dots\dots\dots\dots\dots\dots\dots\dots\dots\dots\dots\dots\dots\dots\dots (19)$$

The ratio of the radial to streamwise components of the bed shear stress is taken to be proportional to the ratio of $\bar{U}/\bar{V}$

$$\tau_{0r} = -\alpha\tau_{\theta\theta} \frac{1}{\bar{V}} \left(\frac{1 - \xi}{\xi} \bar{U} - \bar{U}_t \right) \dots\dots\dots\dots\dots\dots\dots\dots\dots (20)$$

where α = constant.

The radial-plane wall shear stress is expressed in a similar way

$$\tau_{0z}(r_o, r_i) = \beta\tau_{\theta\theta} \frac{w(r_o, r_i)}{\bar{V}} = \frac{1}{4} \rho\beta\gamma f \bar{V}\bar{U} \frac{d}{b} (1 - \xi) \dots\dots\dots\dots (21)$$

where β = constant.

The shear stress $\tau_{\theta z}$ will be expressed by the Boussinesq relation, (11), with ε computed from the power-law velocity distribution with exponent equal to its equilibrium-profile value, $1/n_e$. Thus, the calculated (from the MOM equations) value of n at each section is used for the computation of $\partial v/\partial z$, but the equilibrium-profile value, n_e, is used in the relation for ε

$$\varepsilon = \frac{f\bar{V} d n_e^2}{8(n_e + 1)} (1 - \zeta)\zeta^{(n_e - 1)/n_e} \dots\dots\dots\dots\dots\dots\dots\dots\dots (22)$$

Substitution of (22) into (11) yields

$$\tau_{\theta z} = \frac{1}{8} \rho f \bar{V}^2 \frac{n_e^2}{n_e + 1} \frac{n + 1}{n^2} (1 - \zeta)\zeta^{[(n_e-1)/n_e + (1-n)/n]} \dots\dots\dots\dots (23)$$

The θ-component of the MOM equation is obtained by multiplying each lettered term of (1) by $(z - d/2)$, and each term of (3) by $(r_c - r)$; summing

the results; substituting (14)–(17) for the velocities; substituting (18)–(21) and (23) for the stresses; and integrating the resulting equation over $\zeta = 0$ to $\zeta = 1$, $r = r_i$ to $r = r_o$, and from θ to $\theta + d\theta$. The r-component of the MOM equation is obtained by multiplying each lettered term of (2) by $-(z - d/2)$; making the aforementioned substitutions for the velocities and stresses; and integrating the resulting equation over the control volume indicated previously. The integrations involve lengthy algebra, but are generally straightforward. The resulting simultaneous equations for $\bar{U}$ and n are

$$
\frac{d}{d\theta}\left(\frac{\bar{U}}{\bar{V}}\right)\left[A + B + \frac{1}{3}\gamma(1 - \xi)\right] = -\frac{1}{2(2n + 1)}\frac{d\bar{U}_t}{d\theta} + \frac{n + 1}{2n(n + 2)}
$$

$$
- \frac{1}{3}\gamma\left(\frac{\bar{U}}{\bar{V}}\right)^2\frac{2\xi - 1}{\xi^2}\left(\frac{\xi^2}{2} - \frac{\xi}{2}\right) - \frac{1}{3}\gamma(1 - \xi)\frac{\bar{U}}{\bar{V}}\frac{\bar{U}_t}{\bar{V}}
$$

$$
+ \frac{1}{16}f\left[\alpha\frac{r_c}{d}\left(\frac{\xi - 1}{\xi}\frac{\bar{U}}{\bar{V}} + \frac{\bar{U}_t}{\bar{V}}\right) - 4\beta\gamma\frac{r_c}{b}(1 - \xi)\frac{\bar{U}}{\bar{V}}\right] \dots\dots\dots\dots (24)
$$

and

$$
\frac{1}{2n^2(n + 2)}\frac{dn}{d\theta} = \left(a_1r_c + \frac{1}{6}a_2b^2 + 1\right)\left[(A + B)\frac{\bar{U}}{\bar{V}} + \frac{1}{2(2n + 1)}\frac{\bar{U}_t}{\bar{V}}\right]
$$

$$
+ \frac{1}{6}\gamma(1 - \xi)\frac{n - 1}{n}\frac{\bar{U}}{\bar{V}} - \frac{1}{16}f\frac{r_c}{d}\left(1 - \frac{2n_e^4}{n_e + 1}C\right) \dots\dots\dots\dots (25)
$$

where

$$
A = \frac{1 - 2\xi}{\xi(\xi - 1)}\left[\frac{n(n + 1)}{(2n + 1)(3n + 1)}\xi^{(2n+1)/n} - \frac{n}{2(2n + 1)}\xi^{(n+1)/n}\right] \dots (26)
$$

$$
B = \frac{1}{\xi - 1}\left[\frac{\xi}{2(2n + 1)} - \frac{(n + 1)^2}{2(2n + 1)(3n + 1)}\right] \dots\dots\dots\dots\dots (27)
$$

$$
C = \frac{n + 1}{(nn_e + n_e - n)(2nn_e + n_e - n)} \dots\dots\dots\dots\dots\dots\dots\dots (28)
$$

The coefficients a_1 and a_2 in (25) arise in the least-squares fit of $V(r, \theta)$, obtained from solution of the moment and continuity equations, to a quadratic relation in $(r - r_c)$

$$
\frac{\partial}{\partial r}\frac{V}{\bar{V}} = a_1 + 2a_2(r - r_c) \dots\dots\dots\dots\dots\dots\dots\dots\dots\dots\dots\dots\dots\dots (29)
$$

Depth-Integrated Momentum and Continuity Equations

The depth-integrated θ-momentum and continuity equations are used to compute $V(r, \theta)$ and $U_t(r, \theta)$. The terms on the left side of (2) can be expressed

$$
\rho\left(u\frac{\partial v}{\partial r} + \frac{v}{r}\frac{\partial v}{\partial\theta} + \frac{uv}{r} + w\frac{\partial v}{\partial z}\right) = \rho\left[\frac{\partial}{\partial r}(uv) + \frac{1}{r}\frac{\partial v^2}{\partial\theta} + \frac{uv}{r} + \frac{\partial}{\partial z}(vw)\right]
$$

784

$$- \rho v \left(\frac{\partial u}{\partial r} + \frac{1}{r} \frac{\partial v}{\partial \theta} + \frac{\partial w}{\partial z} \right) \dots \dots \dots \dots \dots \dots \dots (30)$$

Substitution of (4) for the last term of (30), and the result for the left side of (2) yields

$$\rho \left[\frac{\partial}{\partial r} (uv) + \frac{1}{r} \frac{\partial v^2}{\partial \theta} + \frac{2uv}{r} + \frac{\partial}{\partial z} (vw) \right] = \rho g_\theta + \frac{1}{r} \frac{\partial \sigma_{\theta\theta}}{\partial \theta} + \frac{\partial \tau_{\theta z}}{\partial z} \dots (31)$$

For the depth integration of (31), the following relations were adopted.

The velocity and stress relations are given by (14)–(23), with $\bar{V}(\theta)$, $\bar{U}(\theta)$, and $\bar{U}_t(\theta)$, replaced by $V(r, \theta)$, $U(r, \theta)$, and $U_t(r, \theta)$, respectively, to account for their r dependence.

The strength of the secondary rotational flow, $U(r, \theta)$, is radially distributed according to the power law

$$U(r, \theta) = \frac{n_r + 1}{n_r} \bar{U} \left[\frac{r - r_i}{\left(\frac{b}{2} \right)} \right]^{1/n_r} ; \qquad r_i \le r \le r_c \dots \dots \dots \dots \dots (32a)$$

$$U(r, \theta) = \frac{n_r + 1}{n_r} \bar{U} \left[\frac{r_o - r}{\left(\frac{b}{2} \right)} \right]^{1/n_r} ; \qquad r_c \le r \le r_o \dots \dots \dots \dots \dots (32b)$$

where $1/n_r$ = exponent. Note that this assumption results in discontinuities of the r derivatives of the $U(r, \theta)$ profile at $r = r_c$. A value $n_r = 3$ was adopted for this analysis.

The kinematic boundary condition at the channel bed is

$$u \frac{\partial z_b}{\partial r} + \frac{v}{r} \frac{\partial z_b}{\partial \theta} - w = 0; \qquad \text{at } \zeta = 0 \dots \dots \dots \dots \dots \dots (33)$$

where z_b = elevation of the channel bottom.

The corresponding mean-water-surface boundary condition is

$$u \frac{\partial z_w}{\partial r} + \frac{v}{r} \frac{\partial z_w}{\partial \theta} - w = 0; \qquad \text{at } \zeta = 1 \dots \dots \dots \dots \dots \dots (34)$$

where z_w = elevation of the water surface.

Depth integration of (31) after substituting (14)–(23) and (32) for the velocity and stress distributions, and applying the kinematic boundary conditions given by (33) and (34) leads to

$$\frac{(n + 1)^2}{n(n + 2)} \frac{d}{r} \frac{\partial}{\partial \theta} \left(\frac{V}{\bar{V}} \right)^2 + \left[\frac{1}{8} f - \frac{d}{r} \frac{2(n + 1)}{n^2(n + 2)^2} \frac{dn}{d\theta} \right] \left(\frac{V}{\bar{V}} \right)^2 = \frac{1}{\bar{V}^2} g S_0 d$$

$$- \frac{1}{r} (r - r_c) \frac{\partial}{\partial \theta} \left(\frac{d}{r_c} \right) - d \frac{\partial}{\partial r} \left[(D + E) \frac{U}{\bar{V}} + \frac{U_t}{\bar{V}} \right]$$

$$- 2 \frac{d}{r} \left[(D + E) \frac{U}{\bar{V}} + \frac{U_t}{\bar{V}} \right] \dots \dots \dots \dots \dots \dots \dots \dots \dots (35)$$

where S_0 = streamwise bed slope; and

$$D = \frac{1 - 2\xi}{\xi(\xi - 1)} \frac{n}{2n + 1} \quad \dots\dots\dots\dots\dots\dots\dots\dots\dots\dots\dots\dots\dots (36)$$

$$E = \frac{1}{\xi - 1} \left(\xi - \frac{n + 1}{2n + 1} \right) \quad \dots\dots\dots\dots\dots\dots\dots\dots\dots\dots\dots (37)$$

Depth integration of the continuity relation, (4), after making the appropriate substitutions, yields

$$\frac{1}{r} \frac{\partial}{\partial r} (rU_t) = -\frac{1}{r} \frac{\partial V}{\partial \theta} \quad \dots\dots\dots\dots\dots\dots\dots\dots\dots\dots\dots\dots\dots (38)$$

Eqs. (35) and (38) comprise a system of first-order nonlinear partial differential equations for the unknowns $V(r, \theta)$ and $U_t(r, \theta)$.

Numerical Solution

The MOM equations, (24) and (25), were solved for $\bar{U}(\theta)$ and $n(\theta)$; and (35) and (38), the momentum and continuity equations, for $V(r, \theta)$ and $U_t(r, \theta)$. The computations were started approximately one-half to one channel width upstream from the beginning of the channel curve, and extended a like distance beyond the end of the bend. To solve the equations numerically, it was necessary to replace the curvature discontinuities at the ends of the bend by continuous transitions (Olesen 1987);

$$\frac{1}{r_c} = \frac{1}{2r_{ce}} \exp\left(\pi \frac{s}{b} \right); \quad s < 0 \quad \dots\dots\dots\dots\dots\dots\dots\dots\dots (39a)$$

$$\frac{1}{r_c} = \frac{1}{r_{ce}} - \frac{1}{2r_{ce}} \exp\left(-\pi \frac{s}{b} \right); \quad s > 0 \quad \dots\dots\dots\dots\dots\dots (39b)$$

where r_{ce} = the constant centerline radius of the curved channel; and s = centerline distance along the channel measured from the curvature discontinuity. Corresponding relations were used at the downstream end of the curve. It was found in the present study that the results are slightly affected by the decay length [b/π in (39)]. This value was selected after calibration of numerical results using various decay lengths against experimental data.

Eqs. (24) and (25) were solved first, using the Runge-Kutta method, for $\bar{U}(\theta)$ and $n(\theta)$. The initial (far upstream) value of n was obtained from Nunner's (1956) relation:

$$n = n_e = \frac{1}{\sqrt{f}} \quad \dots\dots\dots\dots\dots\dots\dots\dots\dots\dots\dots\dots\dots\dots\dots (40)$$

with f computed for the uniform approach flow. The friction factor, f, was assumed to be constant across the channel. The initial condition on secondary rotational velocity is $\bar{U} = 0$. For the initial solution of these two equations, $\bar{U}_t = 0$ and $\partial(V/\bar{V})/\partial r = 0$ were used. Subsequent iterations used $\bar{U}_t$ obtained from (35) and (38) by averaging the computed U_t across each section; and $\partial(V/\bar{V})/\partial r$ was obtained from (35) and (38) and a least-squares fit of the computed $V(r)$ to

786

$$\frac{V(r)}{\bar{V}} = a_0 + a_1(r - r_c) + a_2(r - r_c)^2 \quad \ldots\ldots\ldots\ldots\ldots\ldots\ldots\ldots\ldots\ldots \quad (41)$$

at each section.

As was noted before, the loss of the r-direction flux of MOM can be so large as to cause the primary velocity profile to become nonmonotonic, with $\partial v/\partial z < 0$ over much of the upper part of the flow. The power-law formulation of v, (14), does not allow for this, and for flows in very sharp bends, n tends to infinity along the curve and the program then would not execute. To prevent this, a maximum value of $n = 100$ was imposed.

The two first-order partial differential equations for $V(r, \theta)$ and $U_t(r, \theta)$, (35) and (38), were solved by a downstream-marching, outward radial, finite-difference scheme, utilizing n and $\bar{U}$ computed from (24) and (25). The upstream boundary condition on V was either a uniform or a power-law distribution across the channel. The computed flow field was found to be insensitive to this boundary condition, provided it is imposed sufficiently far upstream. In the initial solution of (35), $U_t = 0$ was utilized; in subsequent solutions, U_t from the preceding integration of (38) was used. For the calculation of V in (35), n was obtained from the preceding solution of (24) and (25). The computed values of V then were utilized to obtain U_t by integration of (38) outward across the channel. The boundary condition was $U_t(r_i) = 0$. The constancy of streamwise discharge was checked at each section for the computed values of V, which were then adjusted so as to satisfy continuity and prevent error accumulation. Iteration between (35) and (38) was continued until convergence was obtained. Updated solutions for $\bar{U}$ and n then were obtained from (24) and (25), using the V, U_t, and $\partial(V/\bar{V})/\partial r$ computed from (35) and (38). Convergence was judged acceptable when values of $\bar{U}$, n, V, and U_t from successive iterations between (24) and (25), and (35) and (38) did not differ by more than 0.5%. In the computations, $\Delta r = b/20$ and $\Delta\theta = 2$–$5°$ were used. Only about five iterations were required for convergence. The central processing unit (CPU) time was less than 1 s when the program was executed on a Cray X-MP/48.

VERIFICATION AND ANALYSIS

The first step in the verification of the model was evaluation, against experimental data, of the parameters incorporated into it: ξ [(16)], γ [(17)], α [(20)], and β [(21)]. For this purpose, the two vertical-wall fixed-boundary flume flows of Kikuchi et al. (1988), described in Table 1, were selected, because of the detail and completeness of the data reported for them. Optimal conformity of analytical and experimental results, as judged visually from comparative graphs, was obtained for $\xi = 0.5$, $\gamma = 0.3$, $\alpha = 6$, and $\beta = 1$. These values were used in all subsequent computations for both fixed- and erodible-bed bends. The first of these parameters corresponds to a straight u_s profile, which was also adopted by Odgaard (1986, 1989). The constant appearing in the w profile, γ, is a result of w actually not being linearly distributed across the channel, as assumed in (17), and decreasing to zero at the free surface and channel bed.

The strength of the secondary rotational flow as defined and reported by Kikuchi et al. (1988) is

$$q_v = \frac{q}{\bar{V}d_0} \quad \ldots\ldots\ldots\ldots\ldots\ldots\ldots\ldots\ldots\ldots\ldots\ldots\ldots\ldots\ldots\ldots\ldots\ldots\ldots\ldots\ldots\ldots\ldots \quad (42)$$

where $q = \int_0^d |u| \, dz$; $\bar{V}$ and d_0 = mean velocity and depth of the uniform

787

TABLE 1. Flows Used in Evaluation of Constants and Verification of Fixed-Bed Analytical Model

Run number (1)	Channel surface (2)	Bend Radii			θ_o (degrees) (6)	Width b (m) (7)	b/r_c (8)	Discharge (l/s) (9)	Depth d_o (m) (10)	Mean velocity $\bar{V}$ (m/s) (11)	Roughness size (mm) (12)	Friction factor f (13)
		r_o (m) (3)	r_i (m) (4)	r_c (m) (5)								
(a) Kikuchi et al. (1988)												
Run 1	smooth	1.4	1.0	1.2	270	0.4	0.33	7.03	0.0406	0.440	—	0.023
Run 2	rough	1.4	1.0	1.2	270	0.4	0.33	4.80	0.0407	0.302	1.2	0.048
(b) de Vriend et al. (1977)[a]												
T3-1	rough	53	47	50	90	6.0	0.12	610	0.25	0.4	1 ~ 2	0.016
T3-2	rough	53	47	50	90	6.0	0.12	305	0.25	0.2	1 ~ 2	0.031
(c) Rozovskii (1961)												
Run 1	smooth	1.2	0.4	0.8	180	0.8	1.00	12.3	0.060	0.26	—	0.022
Run 8	rough	1.2	0.4	0.8	180	0.8	1.00	12.3	0.063	0.25	3 ~ 4	0.077

[a]The present model was also evaluated against these results, but no comparison is presented herein.
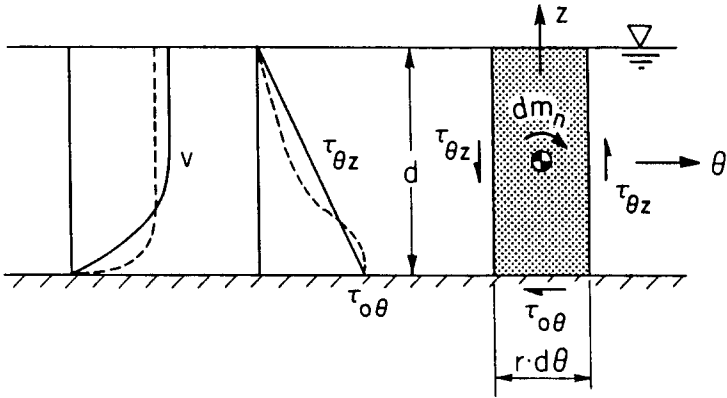
788

FIG. 4. Experimental and Measured Velocity-Profile Exponents (n) for Kikuchi et al.'s (1988) Run 2
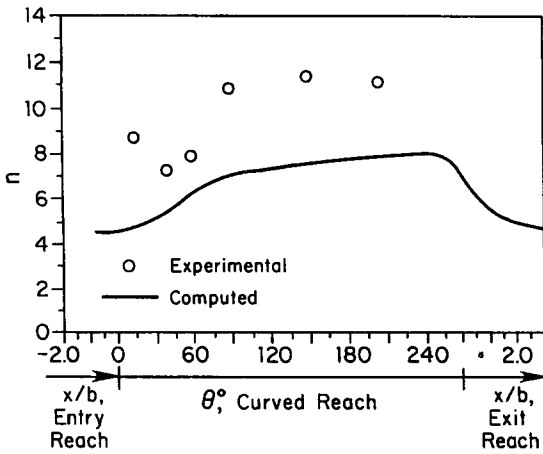

FIG. 5. Experimental and Computed q_u and q_v for Kikuchi et al.'s (1988) Run 2

approach flow; and q_v = normalized strength of the secondary rotational flow. The normalized secondary translational discharge per unit length was defined by them as

$$q_u = q_- + q_+ = \frac{q_1}{\bar{V} d_0} + \frac{q_2}{\bar{V} d_0} \quad \dots\dots\dots\dots\dots\dots\dots\dots\dots\dots\dots (43)$$

where

$$q_1 = \int_0^{d_1} u \, dz \quad \dots\dots\dots\dots\dots\dots\dots\dots\dots\dots\dots\dots\dots (44a)$$

$$q_2 = \int_{d_1}^{d} u \, dz \quad \dots\dots\dots\dots\dots\dots\dots\dots\dots\dots\dots\dots\dots (44b)$$

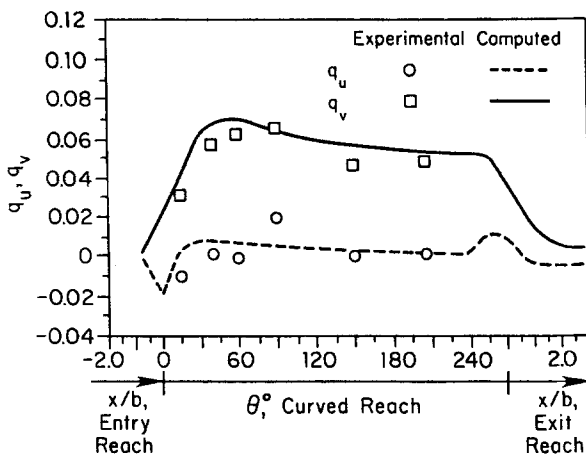in which d_1 = elevation at which $u = 0$. For comparison of measured and

789

FIG. 6. Measured and Computed Lateral Distributions of $V/\bar{V}$ at Representative Sections for Kikuchi et al.'s (1988) Run 2

computed results, Kikuchi et al.'s reported values of q_v and q_u, with the measurements made nearest each vertical wall excluded, were averaged across the section.

Figs. 4–6 show computed and, as available, measured results for Kikuchi et al.'s (1988) run 2. Fig. 4 shows the variation of the computed and measured values of n along the bend. The trend of the n variation is correct, but the experimental values are consistently larger than the computed. Better conformity can be obtained by using for the initial value of n and for the n_e the value determined from the measured upstream primary velocity profiles, instead of n computed from (40). The primary velocity profile is seen to become flatter, which is a result of the loss of r-direction MOM, and not to regain its equilibrium, straight-channel shape until some distance downstream from the end of the bend. Comparisons of computed and measured q_v and q_u are presented in Fig. 5 for run 2. The computed results are seen to be in quite satisfactory agreement with the corresponding reported values; the 30% (approximately) overshoot of the secondary rotational flow velocity above its equilibrium value is accurately predicted by the model. Flows through relatively sharp curves, such as those of Kikuchi et al., portray pronounced changes in the radial distribution of depth-averaged primary velocity, V (see Fig. 6), with the maximum velocity migrating from near the inner bank at the upstream end of the bend, to near the outer bank some distance downstream. Note that the assumption of a power-law radial distribution of U [see (32)] produces a discontinuity of $\partial U/\partial r$ along the channel centerline, which is apparent in the V distributions shown in Fig. 6. The radial redistribution of V along the bend produces a translational discharge, which is toward the inner bank in the upstream transition reach, toward the outer bank further along the bend, and then decays toward zero in the fully developed reach, as can be seen in the q_u distribution shown in Fig. 5. The model also predicted Kikuchi et al.'s run 1 (smooth bed) quite satisfactorily (Yeh 1990).

Several computed solutions were generated to test the sensitivity of the results to the calibration parameters (not shown here, because of the limitation of paper length). It can be concluded that computed q_v is quite sensitive to ξ and α, but somewhat insensitive to γ and β (Yeh 1990).
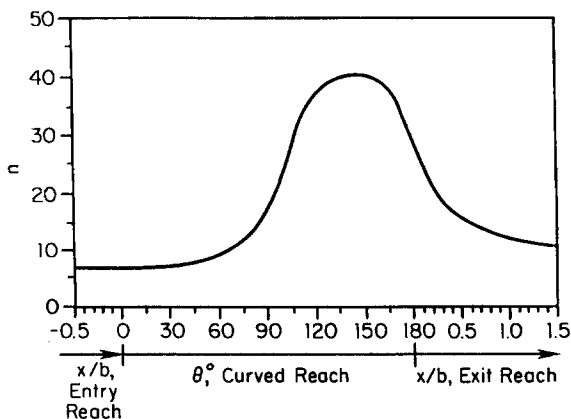
790

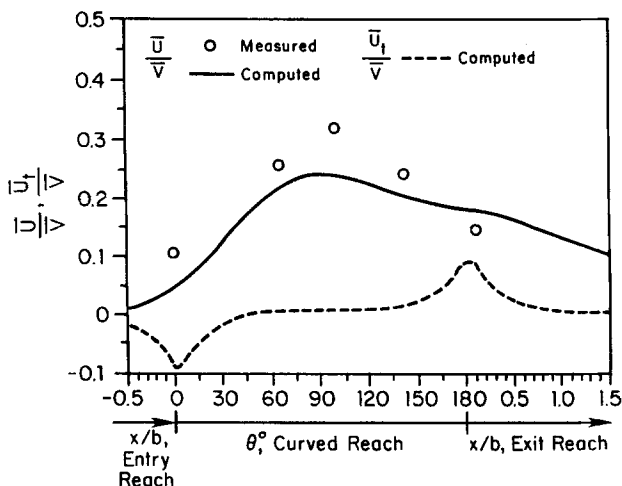**FIG. 7. Computed Streamwise Distribution of n for Rozovskii's (1961) Run 1**

FIG. 8. Measured and Computed $\bar{U}/\bar{V}$, and Computed $\bar{U}_t/\bar{V}$ for Rozovskii's (1961) Run 1

Rozovskii's (1961) runs 1 and 8 (see Table 1) were used to test the model, because both had very sharp bends ($b/r_c = 1$), and one (run 1) had a smooth channel while the other (run 8) had a very rough channel. These flows have been used extensively by other investigators [e.g., Leschziner and Rodi (1979), Johannesson (1988), Shimizu et al. (1990)] for verification of their analytical results. Only the result for run 1 are presented here, in Figs. 7–9.

Due to the strong secondary velocities produced by sharp curvature of the bend, the originally flat shape of the primary-flow velocity profile (especially for run 1) became even flatter (larger n), as can be seen in Fig. 7. Actually, Rozovskii's (1961) measured velocity profiles exhibit strong inversion near the channel walls, with the maximum velocity occurring well below the water surface. The computed normalized secondary velocity, $\bar{U}/\bar{V}$, achieved a maximum value of around 0.2 (which is smaller than the mea-
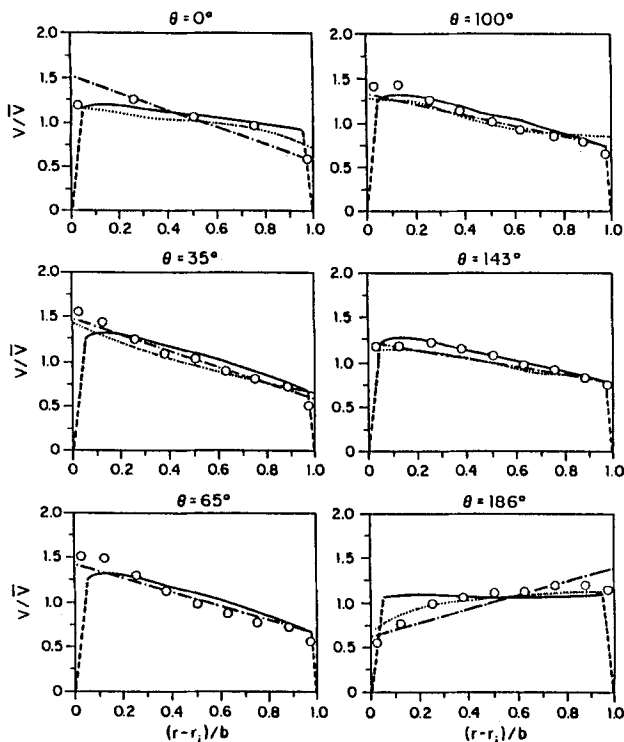
791

FIG. 9. Measured (○); and Computed by Present Model (——), Leschziner and Rodi (1979) (·····), and Johannesson (1988) (·—·—·) $V/\bar{V}$ for Rozovskii's (1961) Run 1

sured 0.3) in both experiments, as can be seen in Fig. 8 for run 1. Note that Rozovskii (1961) plotted the vertical distributions of the secondary-flow velocity for only a few representative cross sections. Some uncertainty surrounds the interpretation of Rozovskii's reported secondary velocities, because their translational and rotational components cannot be separated. Consequently, the comparison of computed and measured secondary rotational velocities must be evaluated with circumspection. It can also be seen in Fig. 8 that this flow has a strong secondary translational velocity due to its sharp channel curvature. Note that the secondary rotational flow does not decay to an equilibrium value, but decreases from the overshoot peak along the full length of the bend. Fully developed flow was not achieved in these runs, because the strong inlet disturbance produced by the sharp curvature of this channel did not decay within the length of the 180° bend. Fig. 9 shows the radial distributions of V for run 1. It can be seen that the thread of maximum velocity remains near the inner wall until near the end of the bend. The cross-channel distortion of streamwise momentum induced along the upstream transition by the radial inclination of the water surface was so strong that the advection of θ momentum toward the outer wall by even the strong secondary velocities of this flow could not shift the maximum V to the outer part of the channel. At the end of the bend, the maximum velocity shifted suddenly toward the outer wall due to the change of channel curvature that produces an ac-

792

celeration of flow in the outer region. The computed results for Rozovskii's run 1 given by Leschziner and Rodi (1979), and by Johannesson (1988) are plotted in Fig. 9 for comparison. It can be seen that all of these computed results are satisfactory along much of the bend lengths.

CONCLUSIONS

A hybrid integral-differential formulation of free-surface nonuniform flow in constant-radius open channels was derived. The generation, overshoot, and decay of the secondary rotational flow, and the interaction of the secondary (rotational and translational) and primary flows, can be clearly explained from consideration of the conservation of fluxes of radial and streamwise (r and θ) moment of momentum within a control volume encompassing an angular segment of the channel. The change the primary velocity profile undergoes as the flow passes along a long bend has been noted in experimental and field data, but heretofore has not been analytically predicted except by three-dimensional numerical simulations of bend flow (Leschziner and Rodi 1979). This striking phenomenon was explained and successfully calculated using the present model based on considerations involving conservation of moment of momentum.

The inverse primary-velocity-profile exponent, $n(\theta)$; increases at the beginning of the bend to a peak and then monotonically approaches its equilibrium value for curved-channel uniform-flow reach. The equilibrium value of n depends on the channel curvature, b/r_c, and its initial value, n_e. The strength of the secondary rotational flow, $\bar{U}(\theta)$, also increases along the upstream part of the bend, attains a maximum value, and then decays monotonically toward its equilibrium value for the curved-channel uniform-flow reach. The overshoot of $\bar{U}(\theta)$ depends on the channel curvature, b/r_c, and surface roughness.

The radial transport of θ momentum by the secondary (rotational and translational) flow usually results in the maximum primary-flow velocity shifting from near the inner wall toward the outer wall along the upstream portion of a bend. However, if a bend is sufficiently sharp [e.g., Rozovskii's (1961) runs 1 and 8], the streamwise momentum gained (lost) at the entrance near the inner (outer) wall due to the sudden radial inclination of the water surface will dominate and the maximum primary-flow velocity will remain within the inner part of the bend along the full length of the bend.

Examination of the values of individual terms in the depth-integrated θ momentum equation obtained from (31) revealed that the relative magnitudes of the terms depend on the sharpness of channel curvature. The term uv/r is usually much smaller than $\partial(uv)/\partial r$ except for very sharp bends. These two terms result in the shift of the thread of maximum primary velocity toward the outer-wall region. The terms $\partial(uv)/\partial r$ and $(1/r)(\partial v^2/\partial \theta)$ increase in magnitude as channel curvature becomes sharper, and can have almost the same magnitude as the gravity and bed-shear force terms, and even be larger than them in the transition reaches. Note that the pressure force in term $(1/r)(\partial\sigma_{\theta\theta}/\partial\theta)$ in (2) plays an important role only in the upstream and downstream transition reaches, where the sudden radial inclination of the water surface gives a θ-momentum impulse to the flow. Further discussion of the relative magnitudes of the momentum-equation terms is presented in the companion paper (Yeh and Kennedy 1993).

of Hydraulic Research, under its EPRIa program. Particular thanks are due to Professor Syunsuke Ikeda, Visiting Professor at IIHR from the Tokyo Institute of Technology in 1988, for his keen insight and invaluable suggestions during key phases of development of the mathematical model.

APPENDIX I.   REFERENCES

Blondeaux, P., and Seminara, G. (1985). "A unified bar-bend theory of river meanders." *J. Fluid Mech.*, 157, 449–470.

de Vriend, H. J. (1976). "A mathematical model of steady flow in curved shallow channels." *Comm. on Hydraulics No. 76-1*, Delft Univ. of Technology, Delft, The Netherlands.

Falcon, M. A., and Kennedy, J. F. (1983). "Flow in alluvial-river curves." *J. Fluid Mech.*, 133, 1–16.

Johannesson, H. (1988). "Theory of river meanders," PhD thesis, University of Minnesota, Minneapolis, Minn.

Johannesson, H., and Parker, G. (1989). "Secondary flow in mildly sinuous channel." *J. Hydr. Engrg.*, ASCE, 115(3), 289–308.

Kikuchi, M., Ikeda, S., and Yamasaka, M. (1988). "A basic study on the three-dimensional flow in a bend." *Proc., 43rd Conf.*, Japan Society of Civil Engineers, Tokyo, Japan, 109–110.

Leschziner, M. A., and Rodi, W. (1979). "Calculation of strongly curved open channel flow." *J. Hydr. Div.*, ASCE, 105(10), 1297–1314.

Nunner, W. (1956). "Wärmeübergang und Druckabfall in rauhen Rohren." *VDI-Forschungsheft 455*, Series B, Band 2 (in German).

Odgaard, A. J. (1986). "Meander flow model. I: Development." *J. Hydr. Engrg.*, ASCE, 112(12), 1117–1136.

Odgaard, A. J. (1989). "River-meander model. I: Development." *J. Hydr. Engrg.*, ASCE, 115(11), 1433–1450.

Odgaard, A. J., and Bergs, M. A. (1988). "Flow processes in a curved alluvial channel." *Water Resour. Res.*, 24(1), 45–56.

Olesen, K. W. (1987). "Bed topography in shallow river bends." *Comm. on Hydr. and Geotech. Engrg. Rep. No. 87-1*, Delft Univ. of Technology, Delft, The Netherlands.

Rozovskii, I. L. (1961). *Flow of water in bends of open channels*. The Israel Program for Scientific Translations, Jerusalem.

Shimizu, Y., Yamaguchi, H., and Itakura, T. (1990). "Three-dimensional computation of flow and bed deformation." *J. Hydr. Engrg.*, ASCE, 116(9), 1090–1108.

Stuiksma, N., Olesen, K. W., Flokstra, C., and de Vriend, H. J. (1985). "Bed deformation in curved alluvial channels." *J. Hydr. Res.*, 23(1), 57–79.

Vadnal, J. L. (1984). "A numerical model for steady flow in meandering alluvial channels," PhD thesis, University of Iowa, Iowa City, Iowa.

Yeh, K. C. (1990). "Flow and bed topography in fixed-channel and river bends," PhD thesis, University of Iowa, Iowa City, Iowa.

Yeh, K. C., and Kennedy, J. K. (1993). "Moment model of nonuniform channel-bend flow. II: Erodible beds." *J. Hydr. Engrg.*, ASCE, 119(7), 796–815.

APPENDIX II.   NOTATION

The following symbols are used in this paper:

A, B, C = constants in (24) and (25);
$d\mathbf{A}$ = inward vector normal to area element dA;
a_1, a_2 = coefficients in (29);
b = channel width;
D, E = constants in (35);
d, d_0 = flow depth; subscript 0 signifies upstream uniform-flow depth;
$\mathbf{e}_r, \mathbf{e}_\theta, \mathbf{e}_z$ = unit vector in r, θ, z directions;

794

dm_n = moment due to nonequilibrium primary-flow velocity profile;
dm_p = pressure moment;
dm_θ = radial-plane acceleration moment;
dm_τ = shear-stress moment;
f = Darcy-Weisbach friction factor;
g = acceleration of gravity;
M_r, M_θ = r and θ components of $\mathbf{M}$, respectively;
$\mathbf{M}$ = MOM across control-volume surface;
$n(\theta)$ = inverse exponent in power-law velocity profile;
n_e = equilibrium inverse exponent in power-law velocity profile;
n_r = inverse exponents in (32);
p = pressure;
q_u, q_v = normalized depth-integrated secondary-flow rotational and translational velocities;
$\mathbf{q}$ = flow-velocity vector in (6);
r, θ, z = components of circular cylindrical coordinate systems;
r_c = channel centerline radius;
r_i, r_o, r_c = radii of curved bend along inner, outer walls, and centerline;
$\mathbf{r}$ = position vector;
S_0 = streamwise bed slope;
$S_s(\theta)$ = radial-water-surface slope;
s = centerline distance along channel;
$U(r, \theta)$ = surface value of linearly distributed secondary rotational velocity, u_s;
$\bar{U}(\theta)$ = section-averaged U;
U_t = depth-averaged u_t;
$\bar{U}_t(\theta)$ = section-averaged u_t;
u, v, w = velocity components in the r, θ, z directions, respectively;
$u_s(r, \theta, z)$ = secondary-flow rotational velocity;
$u_t(r, \theta)$ = secondary-flow translational velocity;
$V(r, \theta)$ = depth-averaged v;
$\bar{V}(\theta)$ = section-averaged v;
x = lateral coordinate for straight channel;
y = streamwise coordinate for straight channel;
z = vertical coordinate;
z_b, z_w = bed and water surface elevations;
α, β = constants in (20) and (21);
γ = constant in (17);
ε = eddy viscosity;
ζ = z/d, origin of z at channel bed;
θ_0 = bend included angle;
ξ = value of ζ at which $u_s = 0$;
ρ = fluid density;
σ_{ii} = $-p + \tau_{ii}$ = normal stress;
τ_{ij} = shear stress; and
τ_{oj} = boundary shear stress.

795